analytical chemistry

pubs.acs.org/ac Article

Peroxymonosulfate Activation on Synergistically Enhanced Single-Atom Co/Co@C for Boosted Chemiluminescence of Tris(bipyridine) Ruthenium(II) Derivative

Zhichao Wu,[⊥] Canglong Wang,[⊥] Zhen Luo, Ying Qin, Xiaosi Wang, Jing Wen, Liuyong Hu,* Wenling Gu,* and Chengzhou Zhu*

Cite This: *Anal. Chem.* 2022, 94, 6866−6873 Read Online

ACCESS | Metrics & More | Article Recommendations | Supporting Information

ABSTRACT: Tris(bipyridine) ruthenium(II)-based luminophores have been well developed in the area of electrochemiluminescence, while their applications in chemiluminescence (CL) are rarely studied due to the poor luminous efficiency and complicated CL reaction. Herein, a novel tris-(bipyridine) ruthenium(II)-based ternary CL system is proposed by introducing cobalt single atoms integrated with graphene-encapsulated cobalt nanoparticles (Co SAs/Co@C) and peroxymonosulfate (PMS) as advanced coreaction accelerator and promising coreactant, respectively. On the basis of the experimental results and density functional theory calculations, it is concluded that Co@C can synergistically modulate the adsorption behavior of PMS on Co SAs and then efficiently activate PMS to produce massive singlet oxygen for remarkable CL emission. Under the optimum conditions, the as-prepared CL biosensor exhibits a good linear range, excellent sensitivity, and selectivity, holding great potential for the practical detection of prostate-specific antigen in human serum.

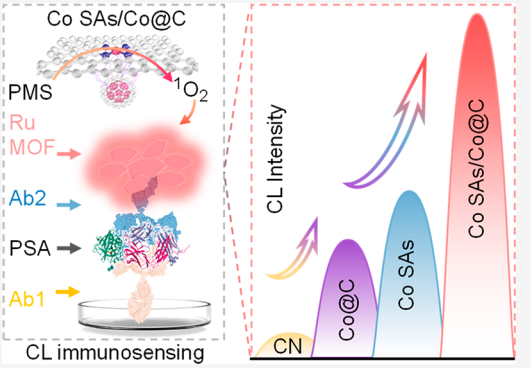

INTRODUCTION

Chemiluminescence (CL) is the light emission process caused by a chemical reaction and is increasingly regarded as a powerful analytical technique.[1,2] In recent years, CL has been widely used in clinical diagnosis and environmental monitoring due to its advantages of high sensitivity, simple operation, low cost, and no need for external light source irradiation.[3−5] Compared with the conventional luminol-based CL systems, tris(2,2′-bipyridyl)-ruthenium(II) {$[Ru(bpy)_3]^{2+}$} and its derivatives are also considered as ideal materials for the construction of biological analysis systems due to outstanding advantages including favorable water solubility, excellent stability, and long excited-state lifetime.[6,7] More importantly, the $[Ru(bpy)_3]^{2+}$-based system has unique properties of reversible regeneration and superior biocompatibility, which provides great promise for further exploration.[8,9] Nevertheless, the depressed efficiency and unsustainable emission of the $[Ru(bpy)_3]^{2+}$-based CL system seriously hinder further applications.[10] Notably, the CL reaction of the $[Ru(bpy)_3]^{2+}$-based system is more complicated; during the reaction, the oxidant and reductant are both indispensable, while only an oxidative reagent is needed for the luminol-based CL system.[11] In general, the advanced oxidation process is a prerequisite to initiating the CL emission of the $[Ru(bpy)_3]^{2+}$-based system, which involves the formation of reactive oxygen species (ROS).[7] Compared with hydroxyl radicals ($^{\bullet}OH$) and sulfate radicals ($SO_4^{\bullet-}$), singlet oxygen ($^1O_2$) shows great potential in the CL field due to its long life, pH tolerance, and high selectivity.[12,13] Consequently, it is urgent to develop novel coreactants and advanced coreaction accelerators with high selectivity and activity to generate $^1O_2$ for the efficient emission of the $[Ru(bpy)_3]^{2+}$-based CL system.

Recently, persulfates, especially peroxymonosulfate (PMS) and peroxydisulfate (PDS), have been reported to generate $^1O_2$ via self-decomposition and catalytic activation.[12,13] Particularly, PMS, a representative persulfate salt with an asymmetric structure ($HO-SO_4^-$), could produce $SO_4^{\bullet-}$ and $^{\bullet}OH$ or $^1O_2$ via the radical or nonradical pathway, respectively, which could act as a promising coreactant in the CL reaction.[14] Nevertheless, it still remains great challenge to identify PMS activation sites and explore underlying catalytic mechanisms, making it difficult to regulate PMS activation with a preferable nonradical pathway for CL reactions. Nowadays, single-atom catalysts (SACs) are considered as one of the most energetic

Received: February 23, 2022
Accepted: April 19, 2022
Published: April 29, 2022

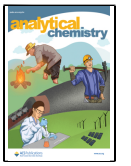

https://doi.org/10.1021/acs.analchem.2c00881
Anal. Chem. 2022, 94, 6866−6873

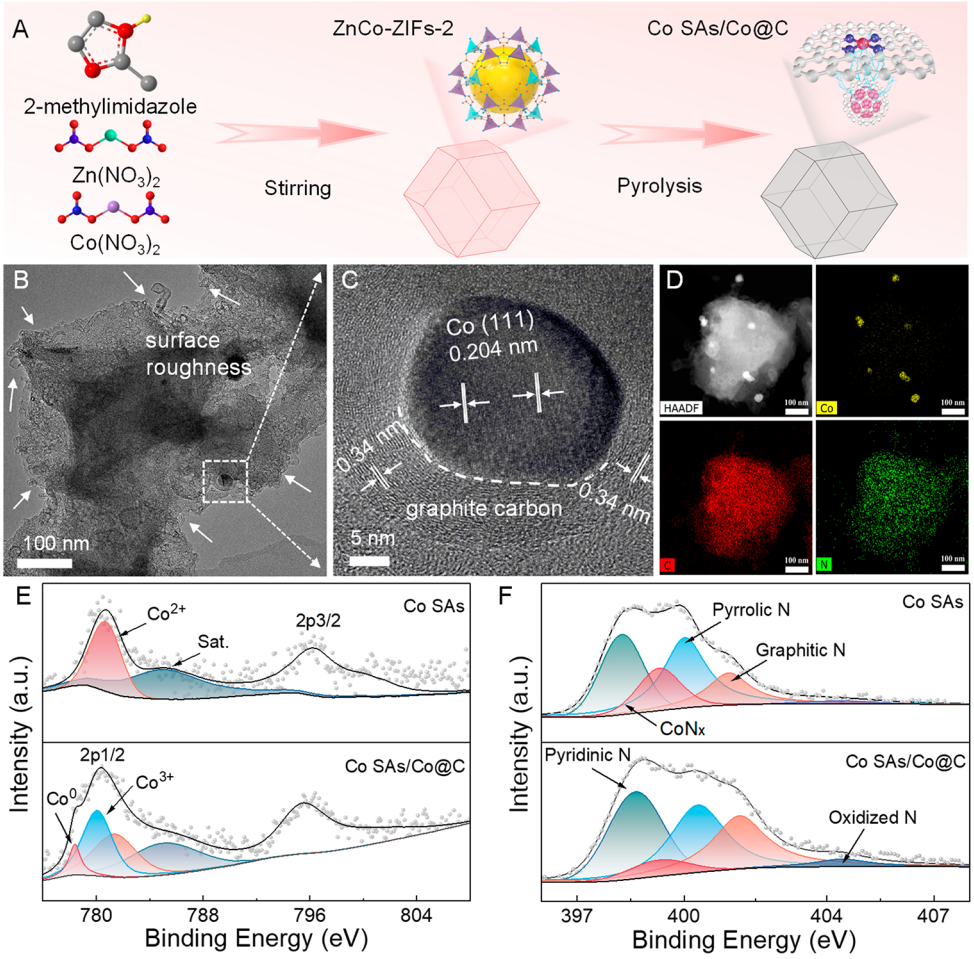

Figure 1. (A) Schematic illustration of the synthesis process of Co SAs/Co@C. (B) TEM image, (C) HRTEM image, and (D) HAADF-STEM image and corresponding EDS element mappings of Co SAs/Co@C. High-resolution XPS spectra of (E) Co 2p and (F) N 1s of Co SAs/Co@C and Co SAs.

research frontiers of heterocatalysis, mainly due to their unique advantages of highly catalytic activity, maximum atom-utilization efficiency, and strong metal−support interaction.[15−17] Compared with the traditional nanocatalysts, the well-defined active sites of SACs provide an ideal platform for studying structure−activity relationships at the atomic level.[18−20] Furthermore, the electronic and geometric structures of central metal atomic sites in SACs can be optimized by introducing synergistic components, which is expected to further improve catalytic activity and selectivity.[21,22] It is expected that appropriate synergistic component additions are available to precisely regulate the adsorption of PMS on active sites and endow PMS activation with the desired pathway. However, the synergistic enhancement effect applied in selective PMS activation for CL systems has rarely been reported.

Herein, an advanced coreaction accelerator of cobalt single atoms combined with cobalt nanoparticles anchored on nitrogen-doped carbon (Co SAs/Co@C) was prepared by the pyrolysis of Co-based metal−organic frameworks (MOFs) (Figure 1A). Density functional theory (DFT) calculations indicate that Co@C can regulate the adsorption behavior of PMS on the active sites of Co SAs to selectively generate more $^1O_2$. Based on the above synergistic effect, CL intensity increased significantly. Notably, the two-dimensional Ru MOF was fabricated by the integration of $[Ru(bpy)_3]^{2+}$ derivatives into the MOF skeleton to avoid the leakage of luminescent reagent during the test (Figure S1). As a proof of concept, a sensitive CL immunoassay of prostate-specific antigen (PSA) was realized by using Ru MOF as the signaling labels. After the sandwich immunocomplexing, the CL intensity linearly increased with the concentration of PSA, displaying a great prospect for practical applications. This work innovatively demonstrates the superiority of SACs and PMS as coreaction accelerators and coreactant in CL system, respectively, opening a new avenue to explore high-performance CL biosensing platforms.

RESULTS AND DISCUSSION

To synthesize cobalt-based SACs, a spatial confining strategy was applied for pyrolyzing the MOF according to the literature.[23] As depicted in Figure 1A and Figure S2, different Co-based zeolitic imidazolate frameworks (ZIFs) were initially prepared with Zn and Co in various molar ratios at room temperature which were then pyrolyzed at high temperature under a N_2 atmosphere to obtain Co SAs/Co@C and Co SACs, respectively. For comparison, a sample of N-doped graphene (N−C) was prepared as well by pyrolyzing Co-free Zn-ZIFs. On one hand, Zn atoms can isolate Co atoms in the geometry, thus preventing the aggregation of cobalt species during pyrolysis. On the other hand, the evaporation of Zn atoms at a high temperature can form few-layered graphite

https://doi.org/10.1021/acs.analchem.2c00881
Anal. Chem. 2022, 94, 6866−6873

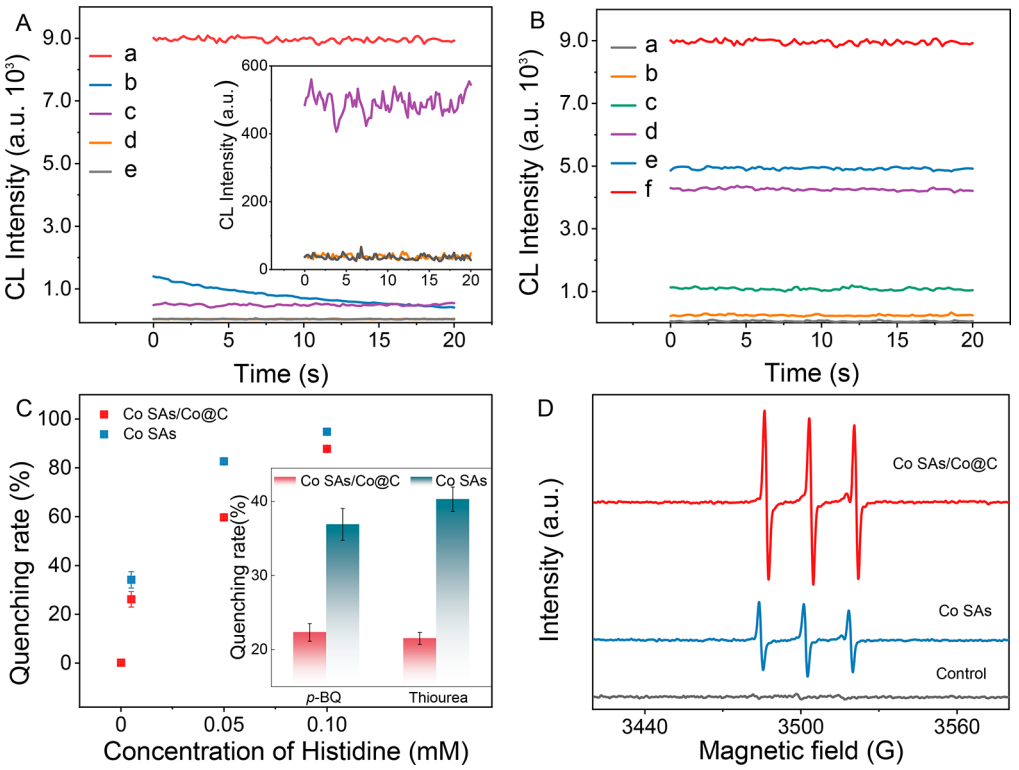

Figure 2. (A) CL kinetic curves of Ru MOF/Co SAs/Co@C using (a) PMS, (b) NaClO, (c) $KMnO_4$, (d) PDS, and (e) H_2O_2 as coreactants. (B) CL curves of (a) PMS, (b) PMS+Ru MOF, (c) PMS+Ru MOF+NC, (d) PMS+Ru MOF+Co@C, (e) PMS+Ru MOF+Co SAs, and (f) PMS+Ru MOF+Co SAs/Co@C. (C) CL intensity quenching rate with different concentrations of histidine (inset: CL intensity quenching rate with *p*-BQ, 2.5 mM; and thiourea, 5.0 mM). (D) EPR spectra characteristic of TEMP-$^1O_2$.

carbon.[24,25] To demonstrate the effectiveness of the spatial confining strategy, transmission electron microscopy (TEM) and high-resolution TEM (HRTEM) images were collected to reveal the detailed morphological and structural features. As shown in Figure 1B and Figure S3B, Co SAs/Co@C cannot maintain the dodecahedron shape of ZnCo-ZIFs (Figure S3A) well after pyrolysis and acid leaching, while the surface roughness changes obviously due to the formation of carbon nanotube-like structures.[26] HRTEM images (Figure 1C and Figure S3C−F) show that the Co nanoparticles are surrounded by few-layered graphite carbon, and the interplanar crystal spacing of the carbon shells is around 0.34 nm, indicating the (002) crystal face of the graphite carbon. Meanwhile, it can be clearly observed that the lattice spacing of the nanoparticles is around 0.204 nm, corresponding to the (111) facet of cobalt nanoparticles.[27] As shown in Figure 1D, the energy-dispersive X-ray spectroscopy (EDS) mapping of Co SAs/Co@C shows that C and N elements are uniformly dispersed over the whole frameworks, while the Co species exist as both single atoms and Co nanoparticles. Furthermore, the element compositions and valence states of the resultant catalysts were analyzed by X-ray photoelectron spectroscopy (XPS). The Co 2p XPS spectrum of Co SAs/Co@C (Figure 1E) presents main peaks at 780.1 and 796.1 eV, confirming the presence of Co^{3+}, while peaks at 781.3 and 797.4 eV correspond to Co^{2+}. The peaks centered at 778.4 and 793.1 eV demonstrated the presence of metallic Co. As shown in Figure 1F, the N 1s XPS spectra could be deconvolved into five peaks at around 398.6, 399.3, 400.3, 401.5, and 404.4 eV, which were ascribed to pyridinic-N, Co−N_x, pyrrolic-N, graphitic-N, and oxidized-N, respectively.[15] It is noteworthy that the XPS results confirmed the existence of Co−N_x in both Co SAs/Co@C and Co SAs samples. Based on the above results and Figures S4−S6, a series of cobalt-based catalysts were successfully obtained and inspired us to further investigate the synergistic enhancement effects on CL.

To prove the superiority of PMS, several coreactants were investigated for reference. The CL kinetic curves of different reactants are displayed in Figure 2A, and the results indicate that the traditional coreactants, including NaClO (curve b), $KMnO_4$ (curve c), PDS (curve d), and H_2O_2 (curve e), exhibit very weak CL intensity. Surprisingly, when PMS (curve a) was introduced into the CL system, a strong and stable CL signal was found, demonstrating its great promise in the CL field. Therefore, PMS was chosen as the efficient coreactant for the CL reaction in the subsequent experiments. Meanwhile, several CL systems with different coreaction accelerators were evaluated to elucidate the role of Co SAs/Co@C in boosting the formation of ROS. As depicted in Figure 2B and Figure S7, compared with the CL reaction without a catalyst (curve b), the addition of N−C (curve c) showed very weak CL emission, while an obvious increase in CL intensity was obtained after using Co SAs (curve d) and Co SAs/Co@C (curve e) as coreaction accelerators. As expected, the CL signal of Co SAs/Co@C is much stronger than those of Co SAs and Co@C, indicating that the synergistic function of large-numbered Co SAs and partial Co@C brings an excellent performance for accelerating the activation of coreactants.

The above research results show that the Ru MOF/Co SAs/Co@C/PMS CL system has a significant improvement in CL emission. To verify the mechanism of this CL system, the influence of radical scavengers on CL intensity was

https://doi.org/10.1021/acs.analchem.2c00881
Anal. Chem. 2022, 94, 6866−6873

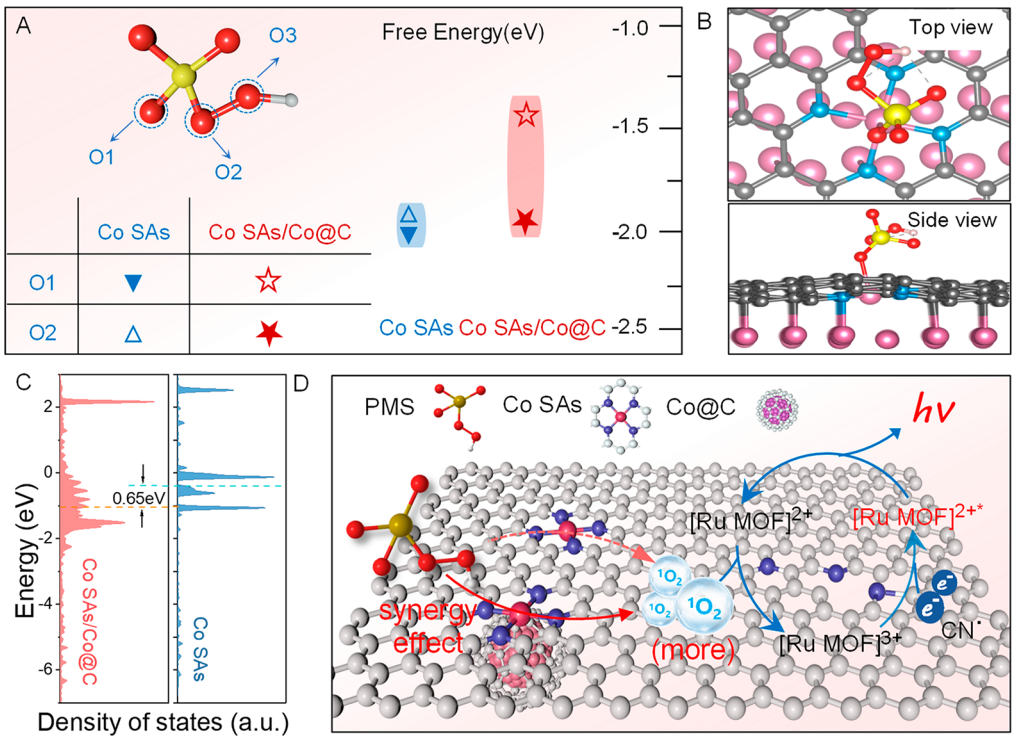

Figure 3. (A) Adsorption energies of PMS onto the different sites of catalysts (inset: molecular model of PMS). (B) Top view and side view of the optimized atomic structures for the O1 site of a PMS molecule on Co SAs/Co@C. (C) Density of states (DOS) for the adsorption process on the catalysts. (D) Possible CL mechanism of the Ru MOF/Co SAs/Co@C/PMS system.

investigated. As displayed in Figure 2C, histidine (an effective scavenger of $^1O_2$), thiourea (an effective scavenger of $OH^•$), and *p*-benzoquinone (an effective scavenger of $O_2^{•-}$) exhibit a quenching effect on the CL intensity, indicating the ROS-mediated CL reaction.[11,28] Notably, histidine exhibits an obvious inhibiting effect on CL intensity, while other scavengers work at 10s of times higher concentration, indicating that $^1O_2$ is the main radical during the CL emission process. Moreover, the quenching results show that the quenching rate of the Co SAs/Co@C CL system is lower than Co SAs under the same concentration of histidine. Therefore, the system with Co SAs/Co@C produced more $^1O_2$ during the CL emission process, which was consistent with the previous difference in luminous intensity. Furthermore, electron paramagnetic resonance (EPR) analysis was performed to verify the reactive radical species by using tetramethyl-4-piperidine (TEMP) and 5,5-dimethyl-1-pyrroline N-oxide (DMPO) as the trapping agents.[11] As presented in Figure 2D, the EPR spectrum shows much stronger signals of the TEMP-$^1O_2$ when Co SAs/Co@C was added, while the signal peak after the addition of Co SAs was much weaker, which further verified the synergistic effect between Co@C and Co SAs in improving the catalytic activity. Meanwhile, only a weak characteristic signal was observed in PMS alone, which might be attributed to the self-decomposition of PMS to generate $^1O_2$. Interestingly, when DMPO was employed as a spin trapping agent to identify $O_2^{•-}$, no obvious signal of the DMPO-$O_2^{•-}$ spin adduct was detected (Figure S8A). This indicates that $O_2^{•-}$ has little effect on the CL intensity, which agreed well with the result that even a very high concentration of *p*-benzoquinone cannot completely inhibit the CL intensity in the previous quenching experiment. At the same time, the classical EPR signals of DMPO-$SO_4^{•-}$and DMPO-$OH^•$ cannot be observed in the system. Instead, a distinct seven-peak signal appeared (Figure S8B), which corresponded to the hyperfine splitting of the oxidation product of DMPO, namely, 5,5-dimethyl-1-pyrrolidone-2-oxyl (DMPO-X).[29] The formation of DMPO-X suggested that highly reactive radical species were generated during PMS activation, causing the fast oxidation of DMPO.[30] Combined with quenching experiments, the results reveal that $^1O_2$ is the main radical involved in the emission process of the CL system, while $OH^•$ and $O_2^{•-}$ contribute little to the CL emission.

To further explore the fundamental insights of the synergy between Co SAs and Co@C for PMS activation in Co SAs/Co@C, density functional theory (DFT) calculations were performed. Accordingly, two structural models, namely, Co SAs and Co SAs/Co@C, were constructed. As shown in Figure 3A, there are two adsorption models of PMS on Co atoms, including O1 and O2 as adsorption sites. Compared with Co SAs, the adsorption free energy of Co SAs/Co@C has a larger gap, indicating that PMS is more inclined to selective adsorption at the single atomic Co site on Co SAs/Co@C. Figure 3B shows the diagrams of the geometrically optimized adsorption configurations, in which strong interaction bonds are formed between the nanoparticles layer and the Co-based active center. As shown in Figure S9, the single atomic Co site adsorbed the O2 site of PMS, which tends to promote the complete spontaneous decomposition of PMS into $SO_4^{•-}$ and $^•OH$.[19,31] In contrast, when the O1 site of PMS is adsorbed on the single atomic Co site, it promotes the decomposition of PMS into $SO_5^{•-}$ by the loss of the H atom. As displayed in Table S1, the O3−H bonds of PMS are elongated from 0.986 Å (Co SAs) to 0.992 Å (Co SAs/Co@C) in the O1−Co models, indicating that it is more feasible for O−H bonds to break for further reaction on Co SAs/Co@C. Moreover, the

https://doi.org/10.1021/acs.analchem.2c00881
Anal. Chem. 2022, 94, 6866−6873

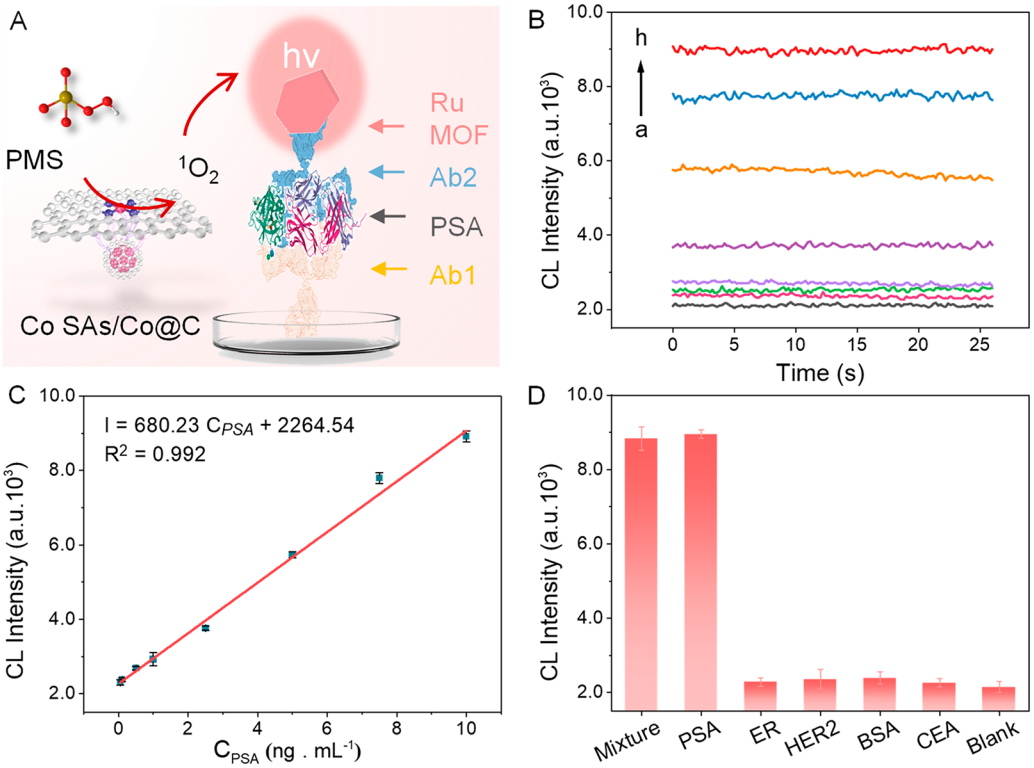

Figure 4. (A) Schematic diagram for the synergistically enhanced CL performances. (B) CL kinetic curves and (C) linear correlation of the Ru MOF/Co SAs/Co@C/PMS CL system for PSA with different concentrations (a−h: 0.05, 0.10, 0.50, 1.00, 2.50, 5.00, 7.50, and 10.00 ng mL^{-1}). (D) CL responses of the proposed detection system with different nonspecific proteins.

adsorption free energies of PMS on single atomic Co sites in Co SAs and Co SAs/Co@C are calculated as −2.18 and −1.42 eV (Table S2), respectively, indicating that the introduction of Co nanoparticles can adjust the surface adsorption capacity of the single atomic Co site. Meanwhile, the weaker adsorption means that the $SO_5^{\bullet-}$ formed by the loss of a H atom is prone to desorption from the single atomic Co site for self-reaction to produce $^1O_2$.[32,33] Furthermore, the d-band centers of the Co in Co SAs and Co SAs/Co@C are calculated in Figure 3C, revealing that the introduction of Co@C downshifts the d-band center by 0.65 eV. For the d-band center theory, a more negative value of the d-band center would lead to a weak interaction between the active site and the adsorbates.[34] Therefore, the trend of weaker binding strength between Co SAs/Co@C and $SO_5^{\bullet-}$ is consistent with the free energy calculation results. As demonstrated above, the Co@C can optimize the adsorption energy of single atomic Co sites, which further promotes the selective production of $^1O_2$ by PMS activation.

Based on the above results and previous literature,[7,28] a possible reaction mechanism for the CL system was proposed as follows (Figure 3D and eqs 1−8). First, $SO_5^{\bullet-}$ tends to be obtained by the loss of H atoms from PMS on Co SAs/Co@C (eq 1), which then produces abundant $^1O_2$ via the following two routes (eqs 2 and 3). As a strong oxidant, $^1O_2$ can react with N-doped graphene (C−N, the support of Co SAs/Co@C) and $[Ru\ MOF]^{2+}$ to form $C{-}N^{\bullet+}$ and $[Ru\ MOF]^{3+}$ (eqs 4 and 5), respectively, indicating that the nitrogen-containing support of Co SAs/Co@C can act as a potential reductant for the $[Ru(bpy)_3]^{2+}$-based CL system. After that, the reductive $C{-}N^{\bullet}$ can be produced via the extremely rapid deprotonation of $C{-}N^{\bullet+}$ (eq 6). Finally, the radiative recombinations of $C{-}N^{\bullet}$ and $[Ru\ MOF]^{3+}$ yield a large number of excited-state $[Ru\ MOF]^{2+*}$ for CL emission (eqs 7 and 8).

$$HSO_5^- \rightarrow SO_5^{\bullet-} + H^+ + e^- \quad (1)$$

Route 1

$$SO_5^{\bullet-} + SO_5^{\bullet-} \rightarrow S_2O_8^{2-} + {}^1O_2 \quad (2)$$

Route 2

$$SO_5^{\bullet-} + SO_5^{\bullet-} \rightarrow 2SO_4^{2-} + {}^1O_2 \quad (3)$$

CL emission

$$C{-}N + {}^1O_2 \rightarrow C{-}N^{\bullet+} + O_2 \quad (4)$$

$$[RuMOF]^{2+} + {}^1O_2 \rightarrow [RuMOF]^{3+} + O_2 \quad (5)$$

$$C{-}N^{\bullet+} \rightarrow C{-}N^{\bullet} + H^+ \quad (6)$$

$$[RuMOF]^{3+} + C{-}N^{\bullet} \rightarrow [RuMOF]^{2+*} + C{-}N \quad (7)$$

$$[RuMOF]^{2+*} \rightarrow [RuMOF]^{2+} + h\upsilon \quad (8)$$

Prostate cancer is the second most common cancer in the world, which is seriously harmful toward the health of males.[35] Prostate-specific antigen (PSA), an oncological marker, is significantly elevated in the serum of patients with prostate cancer.[36] Therefore, ultrasensitive PSA detection at a low serum concentration is of great value for the early diagnosis of prostate cancer. Given the stable and strong CL signal, the application of the ternary CL system was investigated by quantitative biometric determination of PSA (Figure 4A). Under the optimal experimental conditions (Figure S10), the CL response of PSA at different concentrations was monitored.

https://doi.org/10.1021/acs.analchem.2c00881
Anal. Chem. 2022, 94, 6866−6873

As presented in Figure 4B, with an increasing concentration of PSA ranging from 0.05 to 10.00 ng mL^{-1}, the CL intensity was continually enhanced. The variation of CL intensities was obviously proportional to the target concentrations in Figure 4C. The linear regression equation was fitted as $I = 680.23C_{PSA} + 2264.54$ ($R^2 = 0.992$), where I is the CL intensity and C_{PSA} is the concentration of PSA, and the limit of detection was calculated to be 20 pg mL^{-1} (S/N = 3). Additionally, the analytical performance of our proposed method is compared with other reported methods in Table S3, indicating that our proposed method has advantages in linear range and detection limit. As expected, the detection platform based on a ternary CL system has potential value in applications for early disease diagnosis.

In addition, the specificity of the ternary CL system toward target PSA was investigated by employing various interfering proteins including bovine serum albumin (BSA), carcinoembryonic antigen (CEA), estrogen receptor (ER), and human epidermal growth factor receptor-2 (HER2). As observed in Figure 4D, although the concentration of interferers was increased by more than 10-fold for use in the ternary CL system, their CL signals did not exhibit much difference from that of the blank sample. Meanwhile, the CL intensity of the mixture containing target PSA and the four interfering proteins mentioned above presented only slight fluctuations. The results demonstrate that the ternary CL system has excellent selectivity for the detection of PSA. To evaluate the reliability and accuracy of the proposed ternary CL system, actual human serum samples with PSA as the target analyte were tested. As exhibited in Table S4, the recovery values range from 97.31% to 104.66%, and the relative standard deviations are between 2.65% and 5.23%, which provide a superior application prospect for the proposed ternary CL system in clinical PSA detection.

CONCLUSION

In this work, an advanced coreaction accelerator, Co SAs/Co@C, with cobalt nanoparticles synergistically enhancing single cobalt sites was synthesized using a spatial confining strategy. The experimental results and DFT calculations demonstrate that Co@C can contribute to the decomposition of PMS on the active sites of Co SAs via regulating the adsorption behavior of intermediates. Finally, a method for the rapid detection of PSA based on this ternary CL system was established. The method has high sensitivity, low detection limit, and wide linear range. Furthermore, this highly efficient ternary CL system provides great promise for the exploration of advanced coreaction accelerators by optimizing single atomic catalysts with synergistic components.

EXPERIMENTAL SECTION

Synthesis of Zn/Co ZIFs. Typically, $Zn(NO_3)_2{\cdot}6H_2O$ (1.190 g, 4.0 mmol) and $Co(NO_3)_2{\cdot}6H_2O$ (0.582 g, 2.0 mmol) were dissolved in 80 mL of methanol by ultrasonication, and then, 2-methylimidazole (1.968 g, 24 mmol) in 80 mL of methanol was subsequently poured into the above solution for complexation. After the mixture was kept at room temperature for 12 h, the ZnCo-ZIFs-2 with a Zn/Co molar ratio of 2:1 was obtained. The as-obtained precipitates were then collected by centrifugation, washed three times with methanol, and finally dried overnight at 65 °C. Similarly, the ZnCo-ZIFs-8, Co-ZIFs, and Zn-ZIFs were synthesized according to the same procedures by adjusting the Zn/Co molar ratios to 8:1, 0:1, and 1:0.

Synthesis of Co SAs/Co@C, Co SAs, Co@C, and N−C. The as-prepared ZnCo-ZIFs-2 was transferred into a tube furnace and kept at 900 °C for 3 h with a heating rate of 5 °C min^{-1} under N_2 flow. After the tube furnace was naturally cooled to room temperature, the Co SAs/Co@C was obtained. Then, the Co SAs/Co@C was placed in a round-bottom flask and refluxed in H_2SO_4 (3 mol L^{-1}) at 80 °C for 4 h. Finally, the powders were collected after washing to pH = 7 and dried under a vacuum at 65 °C overnight. Similarly, the Co SAs, Co@C, and N−C were synthesized according to the same procedures by pyrolyzing ZnCo-ZIFs-8, Co-ZIFs, and Zn-ZIFs, respectively.

Synthesis of Ru MOF. The synthesis of Ru MOF is described in Figure S2. Briefly, $Zn(NO_3)_2{\cdot}6H_2O$ (18 mg), PVP (40 mg), $Ru(dcbpy)_3^{2+}$(18 mg), and pyrazine (3.2 mg) were mixed in 65 mL of water under ultrasonication. The mixed solution was heated to 80 °C and kept for 24 h. Then, the orange crystals were collected by centrifugation, washed with pure water, and finally redispersed into water for further use.

Preparation of Ab_2-Ru MOF. Briefly, 76.7 mg of 1-ethyl-3-(3-dimethylamino-propyl) carbodiimide hydrochloride (EDC) and 11.5 mg of *N*-hydroxysuccinimide (NHS) were added to the above solution under stirring at 25 °C for 2 h, followed by adding 100 μL of PSA Ab_2 (100 μg mL^{-1}) and shaking overnight at 4 °C. Next, 1 mL of BSA (1%) was added to block the excess binding sites. Then, Ab_2-Ru MOF was collected by centrifugation and stored at 4 °C.

Fabrication of a Ternary CL Immunosensor. 100 μL of Ab_1(1 μg mL^{-1}) was added to a polystyrene microplate and incubated at 4 °C overnight. The microplate was washed several times with PBS. Then, 100 μL of BSA (1%) was added to every well, and the wells were kept at 37 °C for 2 h. After washing three times, the plate was filled with 100 μL of PSA with different contents and incubated for 1 h at 37 °C. Then, the solution was removed, and the microplate was washed three times. Subsequently, 100 μL of Ab_2-Ru MOF was added into each well, and the wells were incubated for 1 h at 37 °C. After removing the solution and washing three times, 110 μL of PBS (0.1 M, pH = 7.4) containing PMS (0.1 M) and 10 μL of Co SAs/Co@C (0.5 mg mL^{-1}) were injected into the microplate to trigger the CL reaction. Then, the CL signal spectrum was recorded for further study.

DFT Calculations. All of the first-principles calculations are performed within the density functional theory (DFT) framework and were implemented using the Vienna Ab-Initio Simulation Package (VASP).[37,38] The ion−electron interaction is described by using the projector augmented-wave (PAW) method.[39] The generalized gradient approximation (GGA) developed by Perdew−Burke−Ernzerhof (PBE functional)[40] was employed to treat the exchange-correlation effect. The 5 × 5 supercell slab models, combined with two layers of a Co (111) plane and one layer of a graphene (001) plane, are employed to calculate the surface properties and adsorption properties. A vacuum length of 15 Å was set to avoid interactions between two adjacent sheets. The DFT-D3 method[41,42] is used to account for the van der Waals correction for all of our calculations. A Gamma-centered *k*-point grid of 3 × 3 × 1 by the Monkhorst−Pack scheme[43] was utilized for Brillouin-zone integration. The plane-wave cutoff energy is set as 520 eV. All atoms are relaxed until the total energy difference and forces on each atom are less than 10^{-6}

https://doi.org/10.1021/acs.analchem.2c00881
Anal. Chem. 2022, 94, 6866−6873

eV and 0.01 eV Å^{-1}, respectively. The adsorption energy of PMS was calculated according to

$$E_{ads} = E_{total} - E_{sub} - E_{PMS}$$

where E_{total} is the total energy of the PMS adsorbed system, and E_{sub} and E_{PMS} are the energies of the substrate and the free PMS, respectively.

■ ASSOCIATED CONTENT

Supporting Information

The Supporting Information is available free of charge at https://pubs.acs.org/doi/10.1021/acs.analchem.2c00881.

Additional experimental details; characterization of Ru MOF, Co SAs/Co@C, Co SAs, and N−C; comparison of different catalyst coreactant accelerators; EPR spectra characteristics; optimized adsorption structure models; experimental condition optimization; bond length and adsorption energy of PMS; comparison of the proposed biosensor for PSA detection; and actual sample analysis (PDF)

■ AUTHOR INFORMATION

Corresponding Authors

Liuyong Hu − *Hubei Key Laboratory of Plasma Chemistry and Advanced Materials, Hubei Engineering Technology Research Center of Optoelectronic and New Energy Materials, Wuhan Institute of Technology, Wuhan 430205, P. R. China*; Email: huly@wit.edu.cn

Wenling Gu − *Key Laboratory of Pesticides and Chemical Biology of Ministry of Education, International Joint Research Center for Intelligent Biosensing Technology and Health, College of Chemistry, Central China Normal University, Wuhan 430079, P. R. China*; Email: wlgu@ccnu.edu.cn

Chengzhou Zhu − *Key Laboratory of Pesticides and Chemical Biology of Ministry of Education, International Joint Research Center for Intelligent Biosensing Technology and Health, College of Chemistry, Central China Normal University, Wuhan 430079, P. R. China*; orcid.org/0000-0003-0679-7965; Email: czzhu@ccnu.edu.cn

Authors

Zhichao Wu − *Key Laboratory of Pesticides and Chemical Biology of Ministry of Education, International Joint Research Center for Intelligent Biosensing Technology and Health, College of Chemistry, Central China Normal University, Wuhan 430079, P. R. China*

Canglong Wang − *Institute of Modern Physics, Chinese Academy of Science, Lanzhou 730000, P. R. China; Advanced Energy Science and Technology Guangdong Laboratory, Huizhou 516000, P. R. China*

Zhen Luo − *Key Laboratory of Pesticides and Chemical Biology of Ministry of Education, International Joint Research Center for Intelligent Biosensing Technology and Health, College of Chemistry, Central China Normal University, Wuhan 430079, P. R. China*

Ying Qin − *Key Laboratory of Pesticides and Chemical Biology of Ministry of Education, International Joint Research Center for Intelligent Biosensing Technology and Health, College of Chemistry, Central China Normal University, Wuhan 430079, P. R. China*

Xiaosi Wang − *Key Laboratory of Pesticides and Chemical Biology of Ministry of Education, International Joint Research Center for Intelligent Biosensing Technology and Health, College of Chemistry, Central China Normal University, Wuhan 430079, P. R. China*

Jing Wen − *Hubei Key Laboratory of Plasma Chemistry and Advanced Materials, Hubei Engineering Technology Research Center of Optoelectronic and New Energy Materials, Wuhan Institute of Technology, Wuhan 430205, P. R. China*

Complete contact information is available at: https://pubs.acs.org/10.1021/acs.analchem.2c00881

Author Contributions

$^{\perp}$Z.W. and C.W. contributed equally.

Notes

The authors declare no competing financial interest.

■ ACKNOWLEDGMENTS

The authors gratefully acknowledge the financial support from National Natural Science Foundation of China (22004042, 22074049, and 22104114), Natural Science Foundation of Hubei Province (2021CFB518 and 2020CFB276), Youth Project of Hubei Provincial Department of Education (Q20211511), the Open Funds of the State Key Laboratory of Electroanalytical Chemistry (SKLEAC202102), the Strategic Priority Research Program of Chinese Academy of Sciences (Grant XDA21010202), the Fundamental Research Funds for the Central Universities (CCNU20QN007 and CCNU20TS013), the Program of Introducing Talents of Discipline to Universities of China (111 program, B17019), and the Advanced Energy Science and Technology Guangdong Laboratory.

■ REFERENCES

(1) Roda, A.; Mirasoli, M.; Michelini, E.; Di Fusco, M.; Zangheri, M.; Cevenini, L.; Roda, B.; Simoni, P. *Biosens. Bioelectron.* **2016**, *76*, 164−179.

(2) Chen, F.; Mao, S.; Zeng, H.; Xue, S.; Yang, J.; Nakajima, H.; Lin, J.-M.; Uchiyama, K. *Anal. Chem.* **2013**, *85*, 7413−7418.

(3) Liu, H.; Su, Y.; Deng, D.; Song, H.; Lv, Y. *Anal. Chem.* **2019**, *91*, 9174−9180.

(4) Saqib, M.; Bashir, S.; Li, H.; Wang, S.; Jin, Y. *Anal. Chem.* **2019**, *91*, 3070−3077.

(5) Liu, Y.; Shen, W.; Li, Q.; Shu, J.; Gao, L.; Ma, M.; Wang, W.; Cui, H. *Nat. Commun.* **2017**, *8*, 1003.

(6) Waite, R. J.; Barbante, G. J.; Barnett, N. W.; Zammit, E. M.; Francis, P. S. *Talanta* **2013**, *116*, 1067−72.

(7) White, H. S.; Bard, A. J. *J. Am. Chem. Soc.* **1982**, *104*, 6891−6895.

(8) Carrara, S.; Arcudi, F.; Prato, M.; DeCola, L. *Angew. Chem., Int. Ed.* **2017**, *56*, 4757−4761.

(9) Sha, H.; Zhang, Y.; Wang, Y.; Ke, H.; Xiong, X.; Xue, H.; Jia, N. *Biosens. Bioelectron.* **2019**, *132*, 203−209.

(10) McDermott, G. P.; Jones, P.; Barnett, N. W.; Donaldson, D. N.; Francis, P. S. *Anal. Chem.* **2011**, *83*, 5453−5457.

(11) Xing, H.; Peng, C.; Xue, Y.; Fan, Y.; Li, J.; Wang, E. *Anal. Chem.* **2020**, *92*, 10108−10113.

(12) Bu, Y.; Li, H.; Yu, W.; Pan, Y.; Li, L.; Wang, Y.; Pu, L.; Ding, J.; Gao, G.; Pan, B. *Environ. Sci. Technol.* **2021**, *55*, 2110−2120.

(13) Shao, P.; Tian, J.; Yang, F.; Duan, X.; Gao, S.; Shi, W.; Luo, X.; Cui, F.; Luo, S.; Wang, S. *Adv. Funct. Mater.* **2018**, *28*, 1705295.

(14) Li, X.; Wang, J.; Duan, X.; Li, Y.; Fan, X.; Zhang, G.; Zhang, F.; Peng, W. *ACS Catal.* **2021**, *11*, 4848−4861.

(15) Li, Z.; Liu, R.; Tang, C.; Wang, Z.; Chen, X.; Jiang, Y.; Wang, C.; Yuan, Y.; Wang, W.; Wang, D.; Chen, S.; Zhang, X.; Zhang, Q.; Jiang, J. *Small* **2020**, *16*, 1902860.

(16) Ji, S.; Chen, Y.; Wang, X.; Zhang, Z.; Wang, D.; Li, Y. *Chem. Rev.* **2020**, *120*, 11900−11955.
(17) Jiao, L.; Xu, W.; Wu, Y.; Yan, H.; Gu, W.; Du, D.; Lin, Y.; Zhu, C. *Chem. Soc. Rev.* **2021**, *50*, 750−765.
(18) Li, X.; Huang, X.; Xi, S.; Miao, S.; Ding, J.; Cai, W.; Liu, S.; Yang, X.; Yang, H.; Gao, J.; Wang, J.; Huang, Y.; Zhang, T.; Liu, B. *J. Am. Chem. Soc.* **2018**, *140*, 12469−12475.
(19) Zhang, L.; Jiang, X.; Zhong, Z.; Tian, L.; Sun, Q.; Cui, Y.; Lu, X.; Zou, J. P.; Luo, S. *Angew. Chem., Int. Ed.* **2021**, *60*, 21751−21755.
(20) Miao, J.; Zhu, Y.; Lang, J.; Zhang, J.; Cheng, S.; Zhou, B.; Zhang, L.; Alvarez, P. J. J.; Long, M. *ACS Catal.* **2021**, *11*, 9569−9577.
(21) Wei, X.; Luo, X.; Wu, N.; Gu, W.; Lin, Y.; Zhu, C. *Nano Energy* **2021**, *84*, 105817.
(22) Wei, X.; Song, S.; Song, W.; Xu, W.; Jiao, L.; Luo, X.; Wu, N.; Yan, H.; Wang, X.; Gu, W.; Zheng, L.; Zhu, C. *Anal. Chem.* **2021**, *93*, 5334−5342.
(23) Han, X.; Ling, X.; Wang, Y.; Ma, T.; Zhong, C.; Hu, W.; Deng, Y. *Angew. Chem., Int. Ed.* **2019**, *58*, 5359−5364.
(24) Ye, L.; Ying, Y.; Sun, D.; Zhang, Z.; Fei, L.; Wen, Z.; Qiao, J.; Huang, H. *Angew. Chem., Int. Ed.* **2020**, *59*, 3244−3251.
(25) Shi, C.; Liu, Y.; Qi, R.; Li, J.; Zhu, J.; Yu, R.; Li, S.; Hong, X.; Wu, J.; Xi, S.; Zhou, L.; Mai, L. *Nano Energy* **2021**, *87*, 106153.
(26) Yin, P.; Yao, T.; Wu, Y.; Zheng, L.; Lin, Y.; Liu, W.; Ju, H.; Zhu, J.; Hong, X.; Deng, Z.; Zhou, G.; Wei, S.; Li, Y. *Angew. Chem., Int. Ed.* **2016**, *55*, 10800−10805.
(27) Wang, A.; Zhao, C.; Yu, M.; Wang, W. *Appl. Catal., B* **2021**, *281*, 119514.
(28) Yan, M.; Ye, J.; Zhu, Q.; Zhu, L.; Xiao, T.; Huang, J.; Yang, X. *Anal. Chem.* **2020**, *92*, 7265−7272.
(29) Verstraeten, S. V. *Inorg. Chim. Acta* **2009**, *362*, 2305−2310.
(30) Stan, S. D.; Daeschel, M. A. *J. Agric. Food Chem.* **2005**, *53*, 4906−4910.
(31) Wu, Z.; Wang, Y.; Xiong, Z.; Ao, Z.; Pu, S.; Yao, G.; Lai, B. *Appl. Catal., B* **2020**, *277*, 119136.
(32) Yermakov, A. N.; Poskrebyshev, G. A.; Stoliarov, S. I. *J. Phys. Chem.* **1996**, *100*, 3557−3560.
(33) Das, T. N. *J. Phys. Chem. A* **2001**, *105*, 9142−9155.
(34) Hammer, B.; Nørskov, J. K. *Surf. Sci.* **1995**, *343*, 211−220.
(35) Jemal, A.; Bray, F.; Center, M. M.; Ferlay, J.; Ward, E.; Forman, D. *CA Cancer J. Clin.* **2011**, *61*, 69−90.
(36) Kingsmore, S. F. *Nat. Rev. Drug Discovery* **2006**, *5*, 310−321.
(37) Kresse, G.; Furthmüller, J. *Phys. Rev. B* **1996**, *54*, 11169−11186.
(38) Kresse, G.; Furthmüller, J. *Comput. Mater. Sci.* **1996**, *6*, 15−50.
(39) Blochl, P. E. *Phys. Rev. B* **1994**, *50*, 17953−17979.
(40) Perdew, J. P.; Burke, K.; Ernzerhof, M. *Phys. Rev. Lett.* **1996**, *77*, 3865−3868.
(41) Grimme, S.; Antony, J.; Ehrlich, S.; Krieg, H. *J. Chem. Phys.* **2010**, *132*, 154104.
(42) Grimme, S.; Ehrlich, S.; Goerigk, L. *J. Comput. Chem.* **2011**, *32*, 1456−1465.
(43) Monkhorst, H. J.; Pack, J. D. *Phys. Rev. B* **1976**, *13*, 5188−5192.

https://doi.org/10.1021/acs.analchem.2c00881
Anal. Chem. 2022, 94, 6866−6873